



OPEN

Kagome van-der-Waals $\text{Pd}_3\text{P}_2\text{S}_8$ with flat band

Seunghyun Park^{1,3}, Soonmin Kang^{1,3}, Haeri Kim¹, Ki Hoon Lee^{1,2}, Pilkwang Kim³, Sangwoo Sim^{1,3}, Nahyun Lee¹, Balamurugan Karuppanan¹, Junghyun Kim¹, Jonghyeon Kim⁴, Kyung Ik Sim⁴, Matthew J. Coak¹, Yukio Noda⁵, Cheol-Hwan Park³, Jae Hoon Kim⁴ & Je-Geun Park^{1,3,6}✉

With the advanced investigations into low-dimensional systems, it has become essential to find materials having interesting lattices that can be exfoliated down to monolayer. One particular important structure is a kagome lattice with its potentially diverse and vibrant physics. We report a van-der-Waals kagome lattice material, $\text{Pd}_3\text{P}_2\text{S}_8$, with several unique properties such as an intriguing flat band. The flat band is shown to arise from a possible compact-localized state of all five $4d$ orbitals of Pd. The diamagnetic susceptibility is precisely measured to support the calculated susceptibility obtained from the band structure. We further demonstrate that $\text{Pd}_3\text{P}_2\text{S}_8$ can be exfoliated down to monolayer, which ultimately will allow the possible control of the localized states in this two-dimensional kagome lattice using the electric field gating.

Over the past two decades, two-dimensional (2D) van-der-Waals (vdW) materials have played an active role in the study of condensed matter physics^{1,2}. Reducing the spatial dimension not only allows the realization of the well-known two-dimensional models like Ising, XY, and Heisenberg models, but also is expected to manifest novel quantum phenomena as in twisted bilayer graphene³. Recently discovered vdW systems with intrinsic magnetic properties^{4–7}: in particular, TMPS_3 (TM = Fe, Ni, Mn)^{8–10}, CrI_3 ¹¹, Fe_3GeTe_2 ¹², and CrGeTe_3 ¹³ have provided an exciting route to understanding the spin-related nanophysics. Nonetheless, exploring 2D magnetic properties is still restricted to few lattice structures, such as triangular or honeycomb structure. Therefore, introducing a new lattice into the still relatively limited collection of materials will be extremely beneficial for the studies on the 2D magnetic materials and its related fields.

Kagome crystal structure is exceptionally rare among the known vdW materials and yet is related to topics in diverse fields of condensed matter physics such as topological insulators¹⁴, the fractional quantum Hall effect^{15–17}, and proposed quantum spin liquids^{18–21}. The exotic properties of kagome lattice originate from their unique structure, a strongly spin-frustrated two-dimensional structure of corner-sharing triangles, as shown in Fig. 1a. Another unique feature originating from this frustrated system is a completely flat band, as in Fig. 1b. The flat band naturally arises from the destructive interference of electron wave functions. It thus represents the localized electrons of compact localized states (CLSs) in real space, as shown in Fig. 1a. A set of CLSs inducing the flat band may superpose with one another without costing any additional energy. The localization of electrons, therefore, is naturally expected to increase the correlation effects^{22–24}, giving rise to unusual phenomena such as fractional quantum Hall effect¹⁵, ferromagnetism^{25,26}, and high T_c superconductivity^{18,27,28}, to name only a few. Once we have a kagome van-der-Waals material that can be cleaved down to monolayer, it will provide an ideal condition for exploring these proposed properties^{24–26}.

The lack of adequate kagome materials has been a bottleneck despite those many fascinating theoretical predictions. Thus, most of the experimental realizations have so far been limited to artificial kagome or bulk kagome systems, which contain 2D kagome embedded in a three-dimensional crystal^{29–36}. Indeed, studies on the bulk kagome materials, including metallic kagome^{31–35}, Herbertsmithite¹⁸, and other metal–organic frameworks³⁶ have been the playground for the exploration into several intriguing electric and magnetic properties of the frustrated systems and topological states. However, the interlayer interaction of these bulk materials, although weak, is likely to mask the very nature of kagome physics and hamper its emergent phenomena³¹. A recent discovery of bulk materials with isolated kagome layers such as FeSn and CoSn also provides an opportunity to examine

¹Center for Correlated Electron Systems, Institute for Basic Science (IBS-CCES), Seoul 08826, Republic of Korea. ²Department of Physics, Incheon National University, Incheon 22012, Republic of Korea. ³Department of Physics and Astronomy, Seoul National University, Seoul 08826, Republic of Korea. ⁴Department of Physics, Yonsei University, Seoul 03722, Republic of Korea. ⁵Institute of Multidisciplinary Research for Advanced Materials, Tohoku University, Sendai 980-8577, Japan. ⁶Center for Quantum Materials, Seoul National University, Seoul 08826, Republic of Korea. ✉email: jgpark10@snu.ac.kr

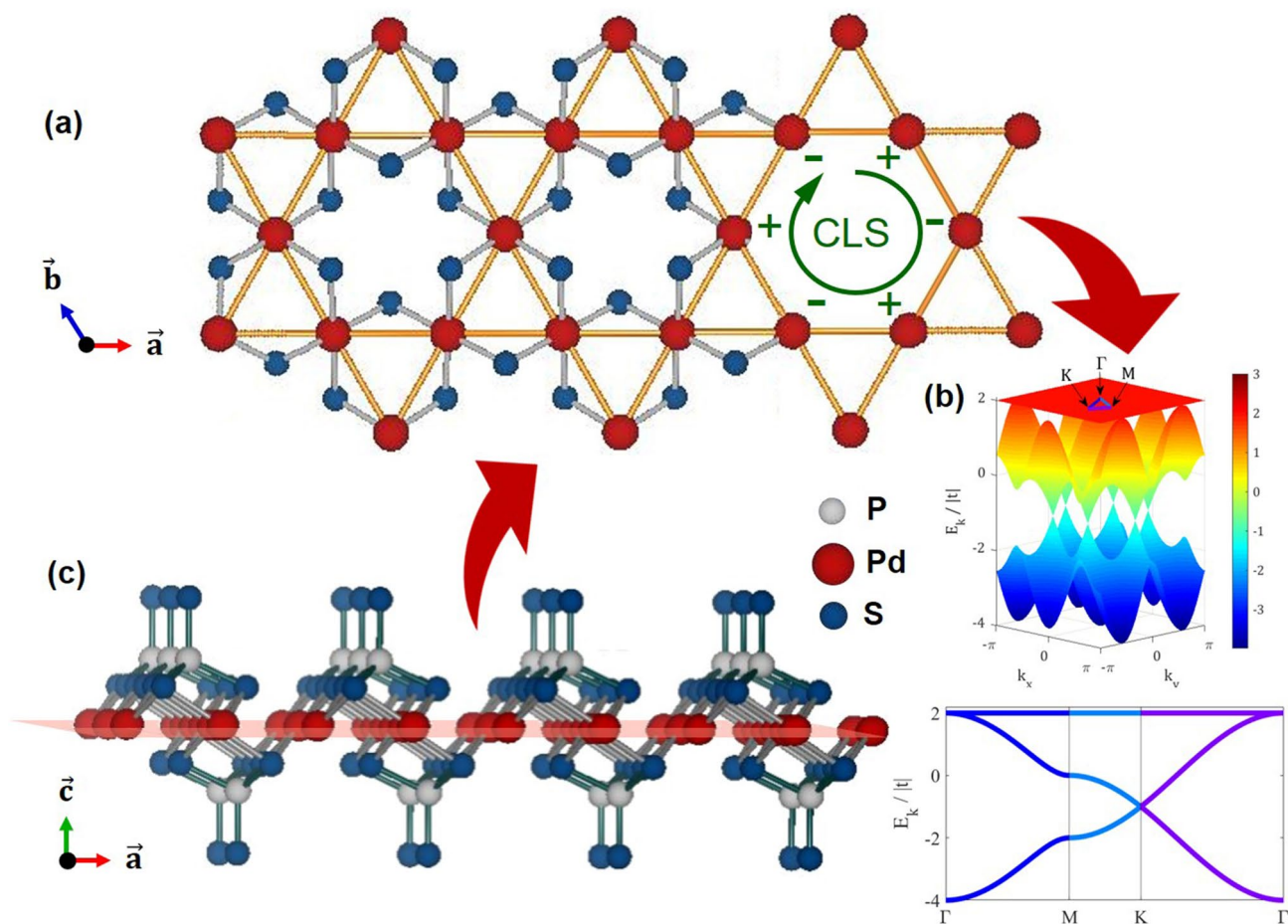


Figure 1. (a) Planar view of the lattice structure of $\text{Pd}_3\text{P}_2\text{S}_8$. The palladium ions form a two-dimensional kagome lattice. (b) The kagome lattice is a geometrically frustrated system and has an inherent flat band structure. The flat band corresponds to a compact localized state known to host correlation effects that introduce topological states. (c) Structure of $\text{Pd}_3\text{P}_2\text{S}_8$ viewed in the ac plane. The structure is slightly tilted to show the configuration of the 2D kagome structure within the plane. The monolayer of the material is illustrated.

the kagome properties using bulk samples^{34,35}. That being said, obtaining a monolayer kagome remains to be a challenge that would offer a fruitful condition. With an isolated kagome layer, one can build nanostructures to modify the electronic structure to study the properties that depends on carrier density, the number of layers, and the orientation of the layers^{3,32,37}.

Here, we report $\text{Pd}_3\text{P}_2\text{S}_8$ as a promising candidate to explore ideal 2D kagome physics. The material can produce a monolayer with the band structures having a very unusual electronic structure of a flat band^{38–40}, which is an exciting property as discussed in other studies^{15–17,22–25}. Our magnetization measurements are in a good agreement with the magnetic susceptibility calculated from the band structure. The nature of the unique flat-band as well as its robustness down to the monolayer is also discussed.

Results

We prepared the samples following the recipes summarized in Method (see Supplementary Fig. S1 online). To check the structure, we carried out both powder and single-crystal X-ray diffraction experiments to confirm that $\text{Pd}_3\text{P}_2\text{S}_8$ forms in the space group of $P-3m1$ (see Fig. 1, and Supplementary Figs. S2, and S3 online)^{41,42}. Afterward, we undertook the susceptibility measurement to find that it exhibits a sizeable diamagnetic response below the room temperature, as shown in Fig. 2a,b⁴³ (see also Supplementary Fig. S4). The diamagnetic behavior is maintained down to the lowest measured temperature. There is a small upturn at much lower temperatures in the data, which is likely to come from the paramagnetic signals of the sample holder and adhesives used. Other than that, there is no hint of any phase transition down to 2 K, giving no reason to suspect any structural or magnetic phase transition over the temperature range of interest. The absence of structural transition can also be verified through heat capacity measurement (see Supplementary Fig. S2 online), which implies that the undistorted kagome lattice is well protected over the temperature range of 2 to 300 K.

The material shows large diamagnetic signals due to the square-planar local structure around Pd ions. There is a small but apparent anisotropic behavior in the susceptibility. The susceptibility is $2.03 \pm 0.38 \times 10^{-4}$ emu/mol for the applied field perpendicular to the ab plane (χ_{\perp}) and $1.75 \pm 0.52 \times 10^{-4}$ emu/mol for the parallel field (χ_{\parallel}). The magnetic anisotropy of the sample is estimated to be about $\chi_{\perp}/\chi_{\parallel} = 1.18 \pm 0.59$. We note that this molar

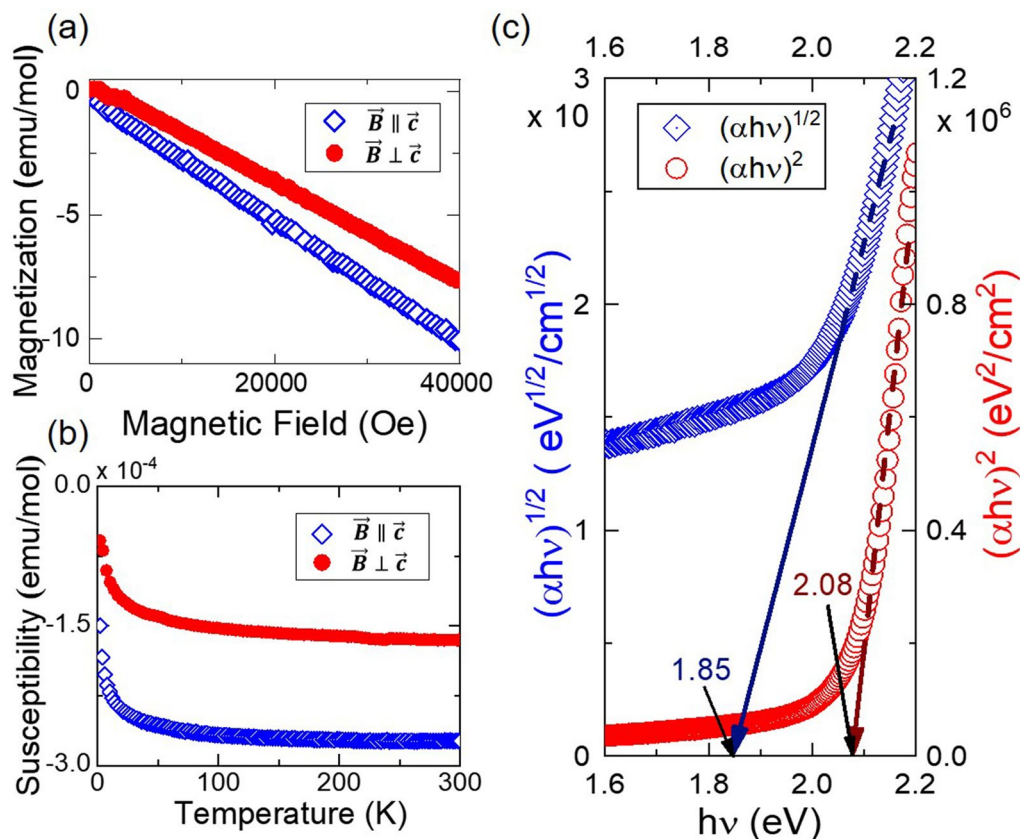


Figure 2. (a) Field sweep and (b) temperature sweep measurement data are presented for the fields perpendicular and parallel to the *ab* plane. The anisotropy of the diamagnetic susceptibility is displayed with the value of 1.18 on average. (open diamond—parallel field; filled circle—perpendicular field). (c) Bandgap estimated from the transmittance data. The estimated fundamental bandgap is about 2 eV using the Tauc plot method. (open diamond— $(\alpha h\nu)^{1/2}$; open circle— $(\alpha h\nu)^2$) α is the absorption coefficient.

susceptibility is similar to bismuth and carbon structures, which exhibit large diamagnetic signals^{44–46}. Based on its insulating property, the diamagnetism of the material should not originate from the dynamics of the conducting charge carriers. Instead, the diamagnetic signals can attribute to the valence electrons of palladium ions which has planar local structure. The susceptibility is in accordance with the value calculated from the electronic band structure, as discussed later.

The optical transmittance measurements are also carried out to examine the electronic structures of $\text{Pd}_3\text{P}_2\text{S}_8$. From the transmittance measurements, we can extract the absorption coefficient and estimate the value of the fundamental bandgap using the Tauc plot method. From the measurement, we expect the fundamental bandgap to be about 2 eV, as shown in Fig. 2c^{47,48}. These basic characterizations of $\text{Pd}_3\text{P}_2\text{S}_8$ are consistent with the electronic band structures that will be presented below.

We examined the band structure of bulk and monolayer $\text{Pd}_3\text{P}_2\text{S}_8$ from first-principles calculations using a density functional theory (DFT) to find the unique electronic properties of this ideal 2D vdW kagome system. The effect of the vdW interactions is reflected in our calculated band structures by employing the experimentally measured lattice parameters. One should note that the vdW functionals used in DFT calculations are usually added to the total energy functional but do not alter the calculated electronic band structure. And the electrons are all paired, so the calculated electronic band structures have no spin labels. The calculated fundamental gap values are determined to be 1.78 and 1.40 eV for monolayer and bulk, respectively. The underestimation of the gap value due to the local approximations for the exchange–correlation interaction is estimated to be about 10%. Regardless of the exchange–correlation functionals adopted, the energy bands obtained from the calculations are very flat, as shown in Fig. 3 and Supplementary Fig. S5 online. The flat band has a significant density of states (DOS) from the Pd *d*-orbitals of the 2D kagome lattice, whose energy is located right below the top valence bands. The Pd-dominant flat band over the whole reciprocal space remains to be robust for the accepted *U* value of ~1.5 eV for Pd atoms, which is a reasonable value according to previous studies⁴⁹. As a further check of the validity of our calculated band structures, we were also able to extract the magnetic susceptibility using the obtained electronic band structures^{50–52}. The calculated diamagnetic susceptibilities are $\chi_{\perp} = 2.38 \times 10^{-4}$ and $\chi_{\parallel} = 2.00 \times 10^{-4}$ emu/mol, respectively, when the field is perpendicular and parallel to the *ab* plane. The corresponding anisotropy ratio is $\chi_{\perp}/\chi_{\parallel} = 1.19$. These values are in good agreement with the experimental results.

For further details, the presence of kagome nature in bulk and monolayer $\text{Pd}_3\text{P}_2\text{S}_8$ can be assessed by examining the band touching at the high-symmetric *k* points. For an ideal kagome lattice, the flat band is expected to

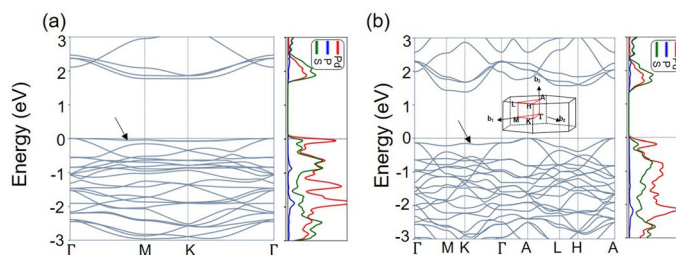


Figure 3. DFT calculation results for (a) the monolayer and (b) bulk crystal. Notably, the top valence band becomes flat as the crystal is exfoliated into monolayer, as shown in (a), due to the weaker interlayer interactions. The projected density of states (PDOS) of palladium is dominant at the flat band.

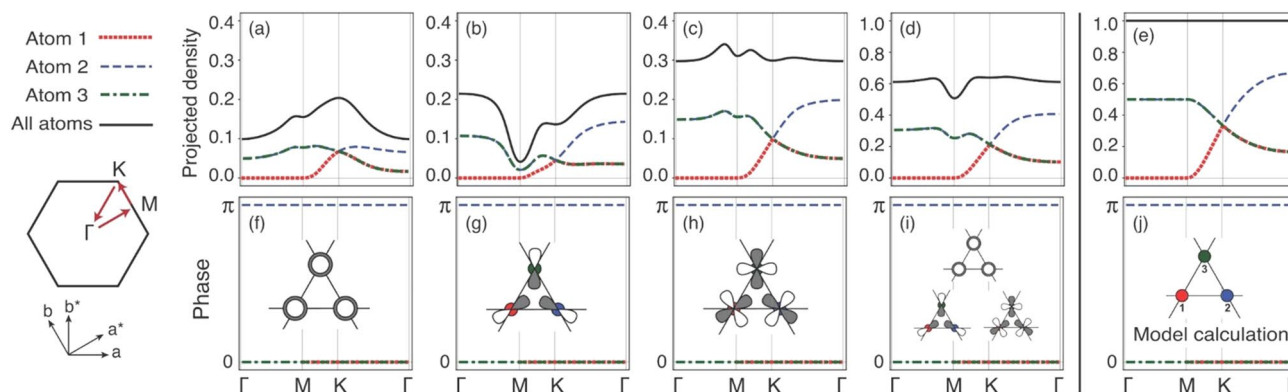


Figure 4. The contributions of (a) d_{z^2} orbital, (b) suitable linear combinations of d_{xz} and d_{yz} orbitals, and (c) appropriate linear combinations of $d_{x^2-y^2}$ and d_{xy} orbitals at each Pd site to the flat TVB. (d) is the total contribution for all d orbitals. A small dip at the M point indicates the hybridization between d orbitals and lower band. Even in the presence of orbital hybridizations, as large as 60% of the flat band comprises the atomic d orbital of Pd. One can see that the projected contributions are very similar to those of (e) ideal kagome model. Each atomic site is indicated by color. (f–i) shows the phase of each orbital. Here, we set the phase of the d_{z^2} orbital at Pd3 to zero. (j) demonstrates the corresponding phases of the kagome model. The phase obtained from our first-principles calculations and those obtained from the model calculation are almost identical.

touch a dispersive band at the Γ point. This band touching at the Γ point is the crucial factor of the undisturbed 2D kagome system. The degeneracy at the Γ point of kagome systems is protected unless there are significant perturbations or disorders^{22,23}. From the projected density of states (PDOS) at the Γ point of the top valence band (TVB), the dominant Pd $4d$ character is confirmed. This band touching can be seen in the band structures of $\text{Pd}_3\text{P}_2\text{S}_8$, confirming the kagome nature.

Finally, the striking flatness of the top valence band (TVB) exists over a wide range of the reciprocal space, especially in the monolayer case. The extreme flatness of TVB can originate from two possible sources; one is a small electron hopping parameter between the atomic sites, and another is the CLS originated from a frustrated kagome structure. However, the large dispersion of the other bands touching the flat band at the Γ point does not support the small-hopping scenario. Thus, the extremely localized electron states representing the flat TVB suggest the presence of the unique nature of kagome lattice, which is the CLS. To rigorously confirm the CLS nature of the flat TVB, we analyzed the wavefunctions of the kagome model as obtained from our DFT calculation⁵³. Figure 4 shows the contribution of Pd d orbitals at each site of the kagome lattice to the TVB and the phase of each orbital. Figure 4d plots the total contribution of each site to the flat TVB of DFT calculations (see also Supplementary Fig. S6 online). The contribution of each site shows similar trend with those of the ideal kagome model throughout the entire Brillouin zone of the Bloch wavevector (see the left column of Fig. 4). In addition, the total contribution of atomic orbitals to the flat TVB is as substantial as 60%. Our first-principles band calculations and the following model calculations of the ideal kagome structure are also in good agreement with each other regarding the phase difference among the orbitals forming the kagome lattice (see Fig. 4f–j). These results are strong evidence reinforcing our view that the flat TVB originates from the kagome structure.

Furthermore, considering that the Pd-dominant flat band is related to the diamagnetic response of the sample, the estimation of an ‘effective’ carrier effective mass over the entire Brillouin zone rather than at a specific wavevector were undertaken. We estimated the ‘effective’ mass, assuming a parabolic function for the energy in terms of the wavevector along each direction in momentum space. The ‘effective’ carrier mass of the bulk along G-K direction is $74.12 m_e$, and $5.65 m_e$ along G-A: where m_e is the intrinsic mass of the free electron.

Moreover, we note that the flat region in the momentum space is wider for monolayer, as shown in Fig. 3. The reduced flatness in the band structure of bulk $\text{Pd}_3\text{P}_2\text{S}_8$ can be understood similarly as mentioned in the

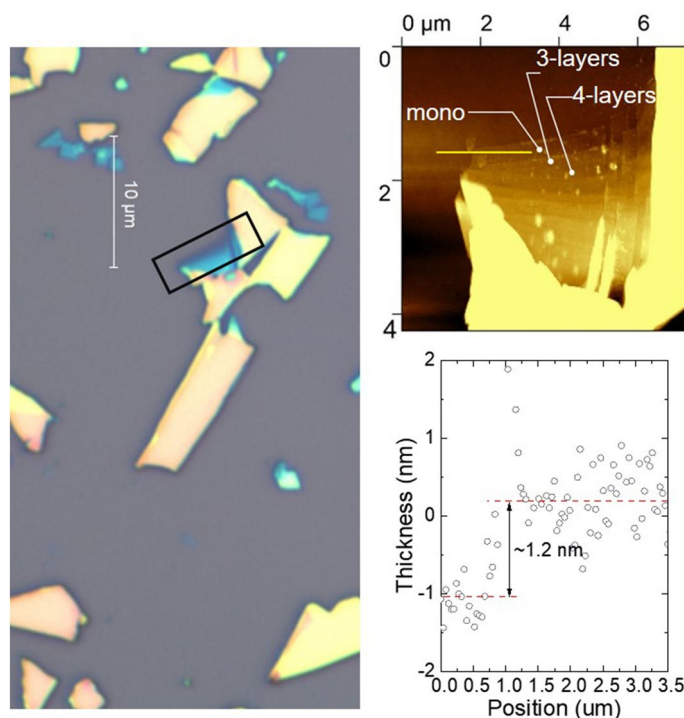


Figure 5. Optical microscope image and AFM scanned image of the flake on 285 nm SiO₂. Additional layers are also seen in the AFM image, forming steps. The yellow line crosses the boundary of the monolayer, and the height difference is about 1.25 nm, as indicated in the figure. The slight bump at the boundary indicates the tape residue on the sample.

recent work of Fe₃Sn₂³¹; the interlayer interaction is likely to interfere with the flat band nature and diminish the character. Therefore, it is likely that the difference between the projected density of states near the TVB of the bulk and monolayer Pd₃P₂S₈ is due to the interlayer interaction.

As an experimental demonstration, we produce monolayer by the mechanical exfoliation method, as shown in Fig. 5. According to our experience, the cleavage energy of Pd₃P₂S₈ seems to be comparable to other S-based magnetic van-der-Waals materials, like NiPS₃⁹. We note that the stability of the material was previously confirmed by theoretical works using the phonon spectrum and ab-initio molecular dynamics calculation³⁸. In this work, we have carried out extensive tests of stability under several conditions. According to our observation, it is stable in the air and shows no sign of degradation under several conditions for 25 h (see Supplementary Fig. S7 online). The availability of the monolayer sample opens up the possibility of examining the flat band physics in the 2D limit by gating experiments.

Discussion. Materials having the kagome lattice have attracted significant interest in the field of condensed matter physics, particularly for its magnetic properties. This geometrically frustrated structure may host exotic spin liquid of phase which electronic version is the flat band in the electronic structure⁵⁴. In this report, we have demonstrated the first ideal kagome vdW material, Pd₃P₂S₈, with transition metal core ions that has strong spin-orbit coupling effect. By comprehensive experimental studies, we have confirmed the ideal kagome lattice remaining intact down to the lowest measured temperature and checked the fundamental physical properties that coincide with the theoretical calculations. By carrying out first-principles calculations, we have found that it also possesses an anomalously flat band at the top of the valence band, which originates from the destructive interference of the kagome lattice. The flat band with possible CLS can host strong electron correlations and give rise to other novel phenomena. The flatness is more extensive in the form of a monolayer as verified by first-principle calculations. The kagome flat band is located near the Fermi level, making it very attractive to modulate the filling portion of the flat band on a real 2D limit by gating experiments^{55,56}. With the potential topological states and emergent magnetism that may be exhibited in the system, Pd₃P₂S₈ will be an attractive platform to address the low-dimensional kagome physics.

Methods

Crystal synthesis. The synthesis of the crystal was done by the chemical vapor transport method with iodine as a transport agent. There were two methods reportedly used to synthesize the crystals. The first method was to use the atomic ratio of 3:2:8 for the Pd, P, and S, respectively. The ingredients (in total 1 g), iodine (0.05 g), and additional sulfur (0.05 g) were ground, mixed, and then sealed in a 20-cm-long quartz tube under a vacuum of lower 10⁻³ torr. Then the quartz tube was placed in a two-zone furnace. Zone 1 was heated to 720 °C for 6 h

and held there for 72 h, while Zone 2 was kept at 690 °C. Subsequently, Zone 1 was cooled to 400 °C for 48 h and maintained there for 6 h; Zone 2 followed the same procedure with the target temperature of 350 °C. Finally, Zone 1(2) was cooled to 150 (120) °C for 6 h before turning to natural cooling to room temperature. The second method is almost identical to the one previously used by Zhang et al.⁵⁷.

Structure analysis. We carried out the structure analysis by measuring both powder and single-crystal samples using two diffractometers. A high-resolution powder diffraction experiment was performed using a commercial powder diffractometer, D8 discover (Bruker), with wavelengths $\lambda_{K\alpha}$ of 1.540590 and 1.544310 Å ($K_{\alpha 1}$ and $K_{\alpha 2}$, respectively) and XtaLAB P200 (Rigaku) with Mo source ($\lambda_{K\alpha} = 0.710747$ Å) was used to identify the structure of the single-crystals. Both results support that our samples form in the space group of P-3m1.

Magnetization measurement. The magnetic susceptibility was measured with a commercial magnetometer (MPMS 3). About 2 ~ 10 mg of samples were used in each measurement and were attached to a quartz sample rod with GE varnish. For the thin samples, a slide cover glass was cut and used for the support. Diamagnetic signals of GE varnish were separately measured to be compared with the signals from the sample. For some measurement sets with the thin glass support, the background signals were subtracted off from the raw data to obtain the pure sample signals and to ensure that the significant signals were from the sample alone. The subtraction was done using the SquidLab software suite, which was developed to improve the fidelity of the signals during this project⁴³. The magnetization was measured in two ways: the field sweeping at a specific temperature and the temperature sweeping with a particular applied field. The temperature sweepings were conducted with an applied field of 1 T, and the field sweepings were conducted at several different temperatures of 2, 50, 100, 150, 200, 250, and 300 K.

Optical measurement. The optical measurements were carried out at 300 K on a grating spectrophotometer (Cary 5000, Agilent) over the spectral range of 190 to 2000 nm (0.62 to 6.5 eV) at a resolution of 1 nm with a spectral bandwidth of 2 nm. The absorption coefficient α was extracted from the transmittance T using Beer's law ($\alpha = -\ln T/d$) where d is the thickness. The single-crystal samples were thinned down by mechanical exfoliation and were fixed by using Kapton tape on Cu sample holders with an aperture of 0.5 mm diameter.

Monolayer exfoliation. The monolayer exfoliation was done onto a SiO₂/Si substrate. We used 285 nm thickness SiO₂ after comparing the optical visibility with other substrates⁵⁸. The substrate was cut to approximately 1 × 1 cm² and was sonicated in isopropanol for 5 min. After blow-drying the substrate, it underwent oxygen plasma treatment with a flow rate of 100 sccm and 300 mT for 10 min to clean the surface⁵⁹. Then the sample was exfoliated by one-sided tape before being placed onto the substrate. When necessary, the tape was very gently rubbed with a cotton swab after being attached to the substrate to eliminate any air bubbles and wrinkles. It was placed on the glass slide for annealing at 85 °C for 1 min, after which the substrate was rapidly cooled with a small amount of acetone sprayed to the back of the glass. The tape was very slowly peeled off from the substrate leaving only a tiny tape residue behind.

Theoretical calculations. The electronic band structure and projected densities of states were calculated using DFT as implemented in the Quantum-ESPRESSO package^{60,61}. Ion–electron interactions were described by the optimized norm-conserving Vanderbilt pseudopotentials^{62,63}, and the exchange–correlation energies were approximated using the Perdew, Burke, Ernzerhof functional⁶⁴. We performed simulations on the monolayers by setting the interlayer distance to 15 Å. We used 8 × 8 × 8 k-point mesh for the bulk crystal and a 12 × 12 × 1 mesh for the monolayer and set the kinetic energy cutoff to 100 Ry. The atomic positions were optimized while fixing the lattice constants to the measured one⁶⁵.

Data availability

Scientific Reports requires the inclusion of a data availability statement with all submitted manuscripts, as this journal requires authors to make available materials, data, and associated protocols to readers.

Received: 3 July 2020; Accepted: 17 November 2020

Published online: 02 December 2020

References

- Geim, A. K. Graphene: status and prospects. *Science* **324**, 1530–1534 (2009).
- Ajayan, P., Kim, P. & Banerjee, K. Two-dimensional van der Waals materials. *Phys. Today* **69**, 38 (2016).
- Iqbal Bakti Utama M., et al. Visualization of the flat electronic band in twisted bilayer graphene near the magic angle twist. *Nat. Phys.* (2020)
- Park, J.-G. Opportunities and challenges of 2D magnetic van der Waals materials: magnetic graphene?. *J. Phys. Condens. Matter* **28**, 301001 (2016).
- Burch, K. S., Mandrus, D. & Park, J.-G. Magnetism in two-dimensional van der Waals materials. *Nature* **563**, 47–52 (2018).
- Gibertini, M., Koperski, M., Morpurgo, A. F. & Novoselov, K. S. Magnetic 2D materials and heterostructures. *Nat. Nanotechnol.* **14**, 408–419 (2019).
- Gong, C. & Zhang, X. Two-dimensional magnetic crystals and emergent heterostructure devices. *Science* **363**, 6428 (2019).
- Lee, J.-U. et al. Ising-type magnetic ordering in atomically thin FeP₃. *Nano Lett.* **16**, 7433–7438 (2016).
- Kuo, C. T. et al. Exfoliation and raman spectroscopic fingerprint of few-layer NiPS₃ Van der Waals crystals. *Sci. Rep.* **6**, 20904 (2016).

10. Lee, S., Choi, K.-Y., Lee, S., Park, B. H. & Park, J.-G. Tunneling transport of mono- and few-layers magnetic van der Waals MnPS₃. *APL Mater.* **4**, 086108 (2016).
11. Huang, B. *et al.* Layer-dependent ferromagnetism in a van der Waals crystal down to the monolayer limit. *Nature* **546**, 270–273 (2017).
12. Deng, Y. *et al.* Gate-tunable room-temperature ferromagnetism in two-dimensional Fe₃GeTe₂. *Nature* **563**, 94–99 (2018).
13. Gong, C. *et al.* Discovery of intrinsic ferromagnetism in two-dimensional van der Waals crystals. *Nature* **546**, 265–269 (2017).
14. Guo, H.-M. & Franz, M. Topological insulator on the kagome lattice. *Phys. Rev. B* **80**, 113102 (2009).
15. Sheng, D. N., Gu, Z.-C., Sun, K. & Sheng, L. Fractional quantum Hall effect in the absence of Landau levels. *Nat. Comm.* **2**, 389 (2011).
16. Neupert, T., Santos, L., Chamon, C. & Mudry, C. Fractional quantum hall states at zero magnetic field. *Phys. Rev. Lett.* **106**, 236804 (2011).
17. Tang, E., Mei, J.-W. & Wen, X.-G. High-temperature fractional quantum hall states. *Phys. Rev. Lett.* **106**, 236802 (2011).
18. Norman, M. R. Colloquium: herbertsmithite and the search for the quantum spin liquid. *Rev. Mod. Phys.* **88**, 041002 (2016).
19. Yan, S., Huse, D. A. & White, S. R. Spin-liquid ground state of the S = 1/2 Kagome Heisenberg antiferromagnet. *Science* **332**, 1173–1176 (2011).
20. Götze, O., Farnell, D. J. J., Bishop, R. F., Li, P. H. Y. & Richter, J. Heisenberg antiferromagnet on the kagome lattice with arbitrary spin: a higher-order coupled cluster treatment. *Phys. Rev. B* **84**, 224428 (2011).
21. Lee, C.-Y., Normand, B. & Kao, Y.-J. Gapless spin liquid in the kagome Heisenberg antiferromagnet with Dzyaloshinskii-Moriya interactions. *Phys. Rev. B* **98**, 224414 (2018).
22. Bilitewski, T. & Moessner, R. Disordered flat bands on the kagome lattice. *Phys. Rev. B* **98**, 235109 (2018).
23. Bergman, D. L., Wu, C. & Balents, L. Band touching from real-space topology in frustrated hopping models. *Phys. Rev. B* **78**, 125104 (2008).
24. Mielke, A. & Tasaki, H. Ferromagnetism in the Hubbard model. *Commun. Math. Phys.* **158**, 341–371 (1993).
25. Tasaki, H. From Nagaoka's ferromagnetism to flat-band ferromagnetism and beyond: an introduction to ferromagnetism in the Hubbard model. *Prog. Theor. Phys.* **99**, 489–548 (1997).
26. Pollmann, F., Fulde, P. & Shtengel, K. Kinetic ferromagnetism on a Kagome lattice. *Phys. Rev. Lett.* **100**, 136404 (2008).
27. Avila, J. *et al.* Flat electronic bands in long sequences of rhombohedral-stacked graphene. *Phys. Rev. B* **97**, 245421 (2018).
28. Pierucci, D. *et al.* Evidence for flat bands near the fermi level in epitaxial rhombohedral multilayer graphene. *ACS Nano* **9**, 5432 (2015).
29. Jo, G.-B. *et al.* Ultracold atoms in a tunable optical Kagome lattice. *Phys. Rev. Lett.* **108**, 045305 (2012).
30. Mohan, P., Nakajima, F., Akabori, M., Motohisa, J. & Fukui, T. Fabrication of semiconductor kagome lattice structure by selective area metalorganic vapor phase epitaxy. *Appl. Phys. Lett.* **83**, 689–691 (2003).
31. Lin, Z. *et al.* Flatbands and emergent ferromagnetic ordering in Fe₃Sn₂ Kagome lattices. *Phys. Rev. Lett.* **121**, 096401 (2018).
32. Ye, L. *et al.* Massive Dirac fermions in a ferromagnetic kagome metal. *Nature* **555**, 638–642 (2018).
33. Yin, J.-X. *et al.* Negative flat band magnetism in a spin-orbit-coupled correlated kagome magnet. *Nat. Phys.* **15**, 443–448 (2019).
34. Kang, M. *et al.* Dirac fermions and flat bands in the ideal kagome metal FeSn. *Nat. Mater.* **19**, 163169 (2020).
35. Kang, M. *et al.* Topological flat bands in frustrated kagome lattice CoSn. *Nat. Commun.* **11**, 4004 (2020).
36. Baidya, S., Kang, S., Kim, C. H. & Yu, J. Chern insulator with a nearly flat band in the metal-organic-framework-based kagome lattice. *Sci. Rep.* **9**, 13807 (2019).
37. de Lima, F. C. & Miwa, R. H. Double flat bands in kagome twisted bilayers. *Phys. Rev. B* **100**, 155421 (2019).
38. Jing, Y. & Heine, T. Two-dimensional Pd₃P₂S₈ semiconductors as photocatalysts for the solar-driven oxygen evolution reaction: a theoretical investigation. *J. Mater. Chem. A* **6**, 23495–23501 (2018).
39. Tang, C. *et al.* Predicting new two-dimensional Pd₃(PS₄)₂ as an efficient photocatalyst for water splitting. *J. Phys. Chem. C* **122**, 21927–21932 (2018).
40. Shan, Y., Li, T. & Liu, L. Electronic structure and optical characteristic for Pd₃P₂S₈ layers. *Solid State Commun.* **306**, 113786 (2020).
41. Calareso, C., Grasso, B. & Silipigni, L. Vibrational and low-energy optical spectra of the square-planar Pd₃(PS₄)₂ thiophosphate. *Phys. Rev. B* **60**, 2333 (1999).
42. Bither, T. A., Donohue, P. C. & Young, H. S. Palladium and platinum phosphochalcogenides: synthesis and properties. *J. Solid State Chem.* **3**, 300–307 (1971).
43. Coak, M. J. *et al.* SquidLab: a user-friendly program for background subtraction and fitting of magnetization data. *Rev. Sci. Instr.* **91**, 023901 (2020).
44. Fukuyama, H. & Kubo, R. Interband effects on magnetic susceptibility. II. Diamagnetism of bismuth. *J. Phys. Soc. Jpn* **28**, 570–581 (1970).
45. Krishnan, K. S. & Ganguli, N. Large anisotropy of the electrical conductivity of graphite. *Nature* **114**, 667 (1939).
46. Sepioni, M. *Magnetic Properties of Graphene* (The University of Manchester, Manchester, 2013).
47. Butler, M. A. Photoelectrolysis and physical properties of the semiconducting electrode WO₂. *J. Appl. Phys.* **48**, 1914 (1977).
48. Dileep, K., Sahu, R., Sarkar, S., Peter, S. C. & Datta, R. Layer specific optical band gap measurement at nanoscale in MoS₂ and ReS₂ van der Waals compounds by high resolution electron energy loss spectroscopy. *J. Appl. Phys.* **119**, 114309 (2016).
49. Östlin, A. *et al.* Electronic structure of palladium in the presence of many-body effects. *Phys. Rev. B* **93**, 155152 (2016).
50. Mauri, F. & Louie, S. G. Magnetic susceptibility of insulators from first principles. *Phys. Rev. Lett.* **76**, 4246 (1996).
51. Laskowski, R. & Blaha, P. Calculations of NMR chemical shifts with APW-based methods. *Phys. Rev. B* **85**, 035132 (2012).
52. Blaha, P. *et al.* *Wien2K: An Augmented Plane Wave + Local Orbitals Program for Calculating Crystal Properties* (Technische Universität Wien, Wien, 2019).
53. Ge, H., Xie, Y. & Chen, Y. d-Orbital-frustration-induced ferromagnetic monolayer Cu₂O₂. *Phys. B* **96**, 085145 (2017).
54. Attig, J. & Trebst, S. Classical spin spirals in frustrated magnets from free-fermion band topology. *Phys. Rev. B* **96**, 085145 (2017).
55. Lee, J., Son, M., Jeong, H., Sim, I. & Myoung, N. Gate-tunable thermoelectric effects in a graphene/WS₂ van der Waals heterostructure. *J. Korean Phys. Soc.* **73**, 940–944 (2018).
56. Chu, D. & Kim, E. K. Recent advances in synthesis and assembly of van der Waals materials. *J. Korean Phys. Soc.* **73**, 805–816 (2018).
57. Zhang, X. *et al.* Lithiation-induced amorphization of Pd₃P₂S₈ for highly efficient hydrogen evolution. *Nat. Catal.* **1**, 460–468 (2018).
58. Blake, P. & Hill, E. W. Making graphene visible. *Appl. Phys. Lett.* **91**, 063124 (2007).
59. Huang, Y. *et al.* Reliable exfoliation of large-area high-quality flakes of graphene and other two-dimensional materials. *ACS Nano* **9**, 10612–10620 (2015).
60. Giannozzi, P. *et al.* I. QUANTUM ESPRESSO: a modular and open-source software project for quantum simulations of materials. *J. Phys. Condens. Matter* **21**, 395502 (2009).
61. Giannozzi, P. *et al.* Advanced capabilities for materials modeling with Quantum ESPRESSO. *J. Phys. Condens. Matter* **29**, 465901 (2017).
62. Hamann, D. R. Optimized norm-conserving Vanderbilt pseudopotentials. *Phys. Rev. B* **88**, 085117 (2013).
63. Schlipf, M. & Gygi, F. Optimization algorithm for the generation of ONCV pseudopotentials. *Comput. Phys. Commun.* **196**, 36–44 (2015).
64. Perdew, J. P., Burke, K. & Ernzerhof, M. Generalized gradient approximation made simple. *Phys. Rev. Lett.* **77**, 3865 (1996).

65. Simon, A., Peters, K., Hahn, H. & Naturforsch, Z. Refinement of crystal structure of tripalladium-di-tetrathiophosphate Pd₃(PS₄)₂ (In German). *Z. Nat. B* **38**, 426–427 (1983).

Acknowledgements

We would like to acknowledge Maxim Mostovoy and Daniel Khomskii for helpful discussions. IBS-CCES was supported by the Institute for Basic Science (IBS) in Korea (Grant No. IBS-R009-G1). J. H. K. acknowledges support by the National Research Foundation of Korea (NRF) grants funded by the Ministry of Science and ICT (MSIT) of Korea (No. 2019R111A2A01062306, No. 2017R1A5A1014862: SRC program (vdWMRC)). Computational resources have been provided by KISTI (KSC-2018-CHA-0051). J.G.P. was supported by the Leading Researcher Program of the National Research Foundation of Korea (Grant No. 2020R1A3B2079375).

Author contributions

J.-G.P. and S.P. conceived the experiments. S.P., S.K., and B.K. synthesized the materials. S.P. and S.K. carried out X-ray diffraction experiments and analyzed data together with Y.N. S.P., N.L., H.K. and S.K. performed the magnetization measurements while S.S. measured the heat capacity. M.J.C. and S.P. carried out the detailed data analysis. S.P. and J. (Junghyun) K. completed monolayer exfoliation. J. (Jonghyeon) K., K.I.S., and J.H.K. performed the optical measurements. P.K. and C.H.P. performed the DFT band calculations. K.L. carried out magnetization calculations and analyzed the experimental data with S.P. S.P., K.L., and J.-G.P. wrote the paper with contributions from all authors.

Competing interests

The authors declare no competing interests.

Additional information

Supplementary information is available for this paper at <https://doi.org/10.1038/s41598-020-77825-1>.

Correspondence and requests for materials should be addressed to J.-G.P.

Reprints and permissions information is available at www.nature.com/reprints.

Publisher's note Springer Nature remains neutral with regard to jurisdictional claims in published maps and institutional affiliations.



Open Access This article is licensed under a Creative Commons Attribution 4.0 International License, which permits use, sharing, adaptation, distribution and reproduction in any medium or format, as long as you give appropriate credit to the original author(s) and the source, provide a link to the Creative Commons licence, and indicate if changes were made. The images or other third party material in this article are included in the article's Creative Commons licence, unless indicated otherwise in a credit line to the material. If material is not included in the article's Creative Commons licence and your intended use is not permitted by statutory regulation or exceeds the permitted use, you will need to obtain permission directly from the copyright holder. To view a copy of this licence, visit <http://creativecommons.org/licenses/by/4.0/>.

© The Author(s) 2020